

Microwave spectroscopy of high- L Rydberg states of neon

R. F. Ward, Jr.

Department of Physics, University of Notre Dame, Notre Dame, Indiana 46556

W. G. Sturuss

Department of Physics, Youngstown State University, Youngstown, Ohio 44555

S. R. Lundeen

Department of Physics, Colorado State University, Ft. Collins, Colorado 80523

(Received 21 April 1995; revised manuscript received 16 August 1995)

Sixteen fine-structure intervals separating $n=10$ neon Rydberg levels with $L=5, 6, 7,$ and 8 were measured with the precision of about ± 0.2 MHz, using fast beam microwave-optical techniques. The measured fine-structure pattern is in good agreement with the predictions of an effective potential model, and this comparison leads to precise determinations of the quadrupole moment and dipole polarizabilities of the $^2P_{3/2}$ ground state of the Ne^+ ion: $Q = -0.204\,03(5)ea_0^2$, $\alpha_s = 1.3028(13)a_0^3$, $\alpha_T = -0.026(5)a_0^3$. The contributions of magnetic interactions to the Rydberg fine structure lead to a determination of the Ne^+ ion's g value, $g_J = 1.354(21)$. All of these core parameters provide challenging tests of atomic structure calculations. The measurements also set a limit on the possible contributions to the fine structure due to a predicted geometric phase effect that is about an order of magnitude smaller than expected.

PACS number(s): 32.30.Bv, 31.10.Dk, 32.10.Fn

All atoms have many Rydberg states with high angular momentum ($L \geq 4$), but there are very few laboratory studies which spectroscopically resolve such states. When data exist on such high- L states, it is likely to result from high-resolution infrared emission spectroscopy. An early study based on such data was carried out by Chang in 1982, who analyzed the structure of some C, O, N, and Ne levels with $L=3$ and 4 [1]. Interest in such high- L states was further stimulated by the discovery of narrow infrared emission lines in the solar spectrum [2] arising from such levels [3]. More recently, high-resolution infrared solar spectra obtained from the ATMOS experiment flown on the space shuttle Challenger has provided more evidence for emission from such high- L Rydberg states of other atoms on the sun, including Fe, Si, Al, and Mg. Theoretical studies of such levels have continued to be carried out by Chang and his collaborators [4,5]. These studies have demonstrated that knowledge of a few parameters characterizing the positive ion core of the Rydberg system, such as the quadrupole moment and dipole polarizabilities, can be used to predict the emission line positions. Unfortunately, these properties cannot yet be calculated with the precision necessary to predict the high- L spectra for arbitrary atoms. It is possible, to some extent, to extract these properties as parameters from analysis of laboratory spectra, but the $L=3$ and 4 levels, for which such laboratory spectra exist, still have small enough L that other complications in the theory, such as residual core penetration and higher-order polarizabilities, complicate this analysis. It would be very desirable to have precise spectra available for even higher- L states, where such complications are minimized, which could be used to extract precise values of the ion core properties. These could then be used both to facilitate precise predictions of high- L Rydberg spectra for the same atom in other regions of the spectrum, and also to stimulate improvements in *a priori* atomic structure calculations of the ionic properties.

Precise laboratory spectroscopy of Rydberg states with $L \geq 4$ has recently been achieved for the helium atom [6] and for the closely analogous H_2 molecule [7], using fast beam microwave-optical techniques. The same experimental techniques can also be used to study other atomic systems with stable positive ions, and in this way provide laboratory data to complement the studies of natural high- L sources described above. In the study reported here, we have used these methods to study the fine structure of high- L Rydberg states of atomic neon. Neon was chosen because careful studies of its $L=3$ and 4 states already exist [1,8], a circumstance which should clarify the impact of the very high- L measurements of this study.

Figure 1 shows the apparatus used for this study. A beam of Ne^+ ions of energy 25 KeV were obtained from a small ion source [9] and neutralized in a gas charge exchange cell containing a few mTorr of air to obtain a fast neutral beam of neon. Neon atoms formed in $n=10$ Rydberg levels were selectively detected using a Doppler-tuned CO_2 laser at 4 in Fig. 1, which excites them to the $n=27$ level, from which

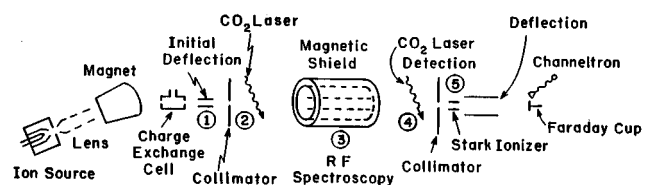


FIG. 1. Schematic diagram of fast beam microwave-optical apparatus. The fast neon beam is formed by neutralizing a 25-KeV Ne^+ beam in a charge-exchange cell. Residual ions are deflected out of the beam at 1. Selective detection of particular $n=10$ neon Rydberg levels is achieved using a Doppler-tuned CO_2 laser at 4 to excite $10 \rightarrow 27$ transitions, after which $n=27$ atoms are Stark ionized at 5, and the ion current collected in a channeltron. The similar laser interaction region at 2 is used to insure a population difference for the microwave transition, driven at 3.

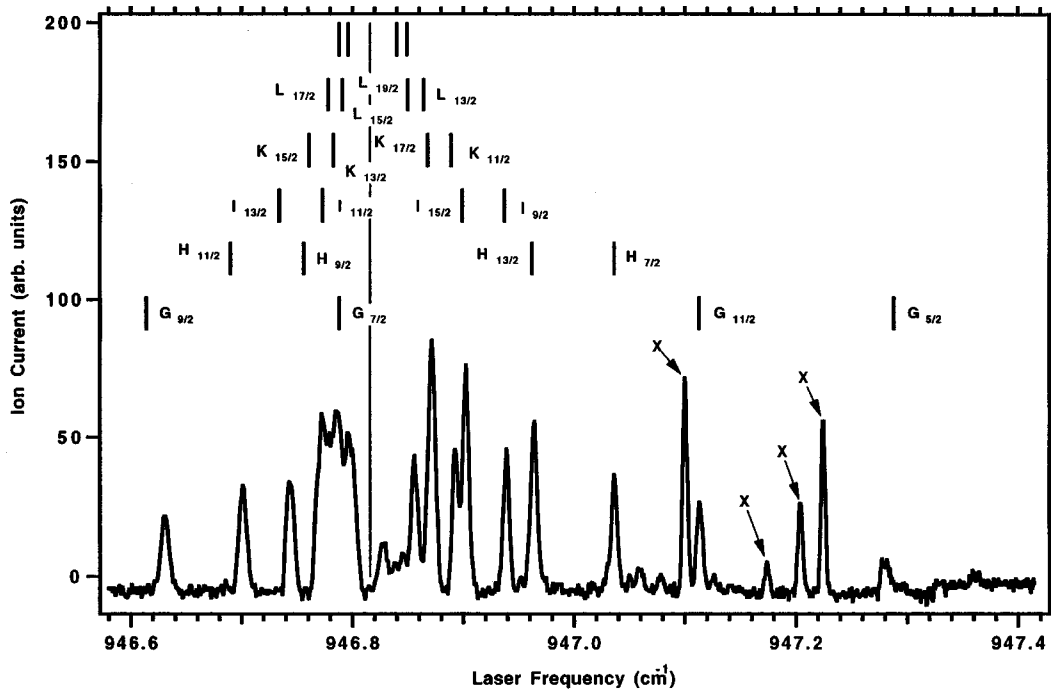


FIG. 2. Stark-ionization current observed as a function of the Doppler-tuned laser frequency, near the frequency of hydrogenic 10-27 transitions, 946.816 cm^{-1} . Individual peaks represent excitation of particular high- L $n=10$ neon Rydberg levels, resolved in frequency as a consequence of the $n=10$ Rydberg fine structure. Many of the peaks can be identified by reference to the $n=10$ level structure, which is plotted above the spectrum using the same energy scale. The solid vertical line corresponds to the hydrogenic 10-27 transition frequency, and to the hydrogenic Rydberg binding energy in the level diagram. The fine-structure level labels, e.g., $H_{9/2}$ are an abbreviation of the $(J_c)nL_K$ nomenclature discussed in the text. The four unidentified lines labeled X are not 10-27 transitions.

they are immediately Stark ionized. The resulting ion current is collected in a Channeltron electron multiplier. The CO_2 laser is operated on one of its discretely tuneable lines, typically $P(18)$ at 945.980 cm^{-1} , but as the angle of intersection of this laser with the fast neon beam is varied, the apparent laser frequency seen by the neon atoms is Doppler tuned smoothly through the interval representing the $n=10$ neon fine-structure energies. When the Stark-ionized current is plotted as a function of the Doppler-tuned laser frequency, a well-resolved optical spectrum is obtained, as illustrated in Fig. 2. Each peak in this spectrum (except for the four peaks marked "X" [10]) represents the excitation of a particular $n=10$ fine-structure level to $n=27$. The qualitative pattern of the spectrum can be understood by noting that, neglecting the (small) fine structure of the $n=27$ levels, the optical spectrum is a direct map of the positions of these $n=10$ neon Rydberg levels, with more tightly bound $n=10$ occurring at higher excitation energies. This is emphasized in Fig. 2 by including a level diagram of these $n=10$ high- L neon levels, drawn with the same energy scale. These levels are characterized by the total angular momentum of the ion core (J_c), the Rydberg electron state (n, L), and by the value of

$$\vec{K} = \vec{J}_c + \vec{L},$$

and we denote them by

$$(J_c)nL_K.$$

Most of the well-resolved lines in the optical spectrum are implicitly identified by the correspondence with the level diagram and the selection rules $\Delta J_c = 0$ and $\Delta L = \Delta K = 1$.

For example, the line at 947.04 cm^{-1} represents excitation of the $(\frac{3}{2})10H_{7/2}$ level to the $(\frac{3}{2})27I_{9/2}$ level. In order to identify the optical lines, an initial estimate of the $n=10$ level structure was carried out with the effective potential model discussed below, using previous estimates of the core parameters, Q , α_s , and α_T .

The experimental spectrum of Fig. 2 shows only Rydberg levels bound to the $^2P_{3/2}$ state of Ne^+ , and not to the higher-energy $^2P_{1/2}$ state. This is in contrast to observations of similar lines in atomic carbon [11], where both types of lines are clearly observed. A plausible explanation of their absence in neon is autoionization of the $n=27$ level. Since $n=27$ Rydberg levels bound to the $P_{1/2}$ core state of neon, whose excitation energy is $780.424(1) \text{ cm}^{-1}$ [12], are unstable against autoionization, they may, and apparently do, decay before reaching the Stark ionizing field. The transit time between laser and ionizer is approximately $0.6 \mu\text{s}$.

Transitions between particular pairs of $n=10$ Rydberg levels were studied with much higher resolution using microwave spectroscopy. The method is the same as that used in previous studies of helium and H_2 [6,7]. For example, to study the $10H_{11/2} - 10I_{13/2}$ transition, the laser at 4 in Fig. 1 was tuned to excite and detect the $10H_{11/2}$ state, using the well-resolved line at approximately 946.7 cm^{-1} . If a microwave transition between the $10H_{11/2}$ and $10I_{13/2}$ states is induced in the region at 3 in Fig. 1, this will generally result in a change in the population of the $10H_{11/2}$ state, and consequently a change in the Stark ionization current. Since the only transitions which will have this effect are those involving the $10H_{11/2}$ state, identifying a microwave transition is relatively simple, and follows from the identifications of the

TABLE I. Transitions are between two $n=10$ levels identified in column 2 by the values of L and K . Column 3 gives the fitted “spinless” transition frequency, and the geometric average of parallel and antiparallel rf propagation directions. Columns 4, 5, and 6 show standard deviation uncertainties from the fit statistics, unresolved magnetic fine structure, and stray electric fields, respectively, with the quadrature sum of these in column 7. All values are in MHz.

	Transition	ν_0	$\Delta\nu(\text{fit})$	$\Delta\nu(\text{MFS})$	$\Delta\nu(E)$	$\Delta\nu(\text{tot})$
(1)	$H_{11/2}-I_{13/2}$	1342.144	0.041	0.068	0.010	0.080
(2)	$I_{13/2}-K_{15/2}$	800.524	0.022	0.046	0.000	0.051
(3)	$K_{15/2}-L_{17/2}$	494.036	0.018	0.032	0.040	0.054
(4)	$H_{9/2}-I_{11/2}$	210.705	0.024	0.039	1.130	1.131
(5)	$I_{11/2}-K_{13/2}$	290.113	0.016	0.031	0.220	0.223
(6)	$K_{13/2}-L_{15/2}$	236.680	0.020	0.024	0.010	0.033
(7)	$H_{13/2}-I_{15/2}$	1890.884	0.028	0.114	0.010	0.118
(8)	$I_{15/2}-K_{17/2}$	926.351	0.018	0.069	0.010	0.072
(9)	$K_{17/2}-L_{19/2}$	511.594	0.011	0.045	0.070	0.084
(10)	$I_{9/2}-K_{11/2}$	1429.088	0.013	0.024	0.000	0.027
(11)	$K_{11/2}-L_{13/2}$	764.916	0.016	0.019	0.040	0.047
(12)	$I_{13/2}-K_{13/2}$	1446.936	0.029	0.074	0.070	0.106
(13)	$K_{15/2}-L_{15/2}$	883.085	0.036	0.051	0.060	0.087
(14)	$H_{9/2}-I_{9/2}$	5123.579	0.075	0.065	0.890	0.896
(15)	$I_{11/2}-K_{11/2}$	3481.761	0.063	0.049	0.240	0.253
(16)	$I_{15/2}-K_{15/2}$	4131.356	0.038	0.120	0.070	0.145

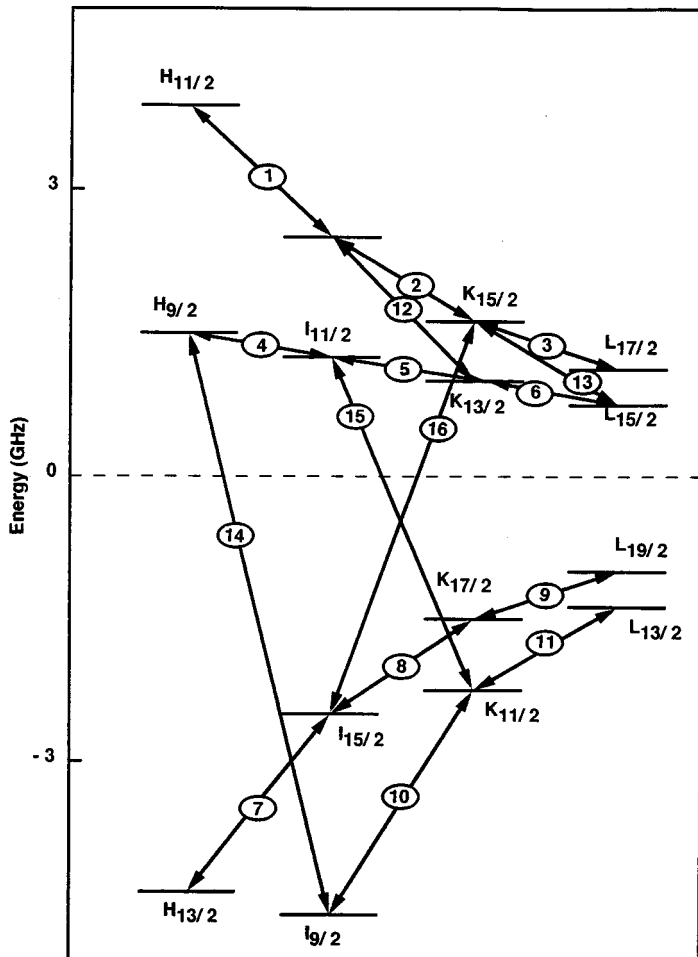


FIG. 3. Level diagram showing the 15 $n=10$ Rydberg levels of neon, whose relative positions are determined by the 16 microwave interval measurements reported here. The numbered transitions refer to Table I, in the text.

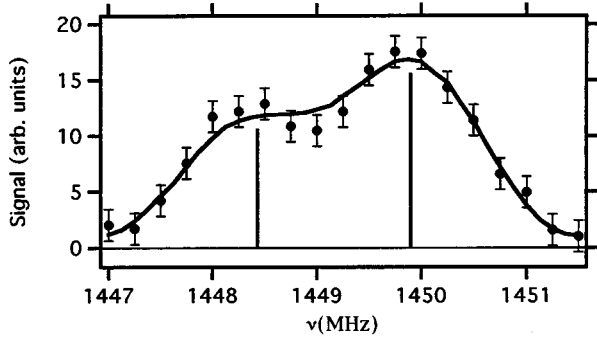


FIG. 4. Microwave resonance signal for $10I_{13/2}-10K_{13/2}$ transitions in neon, measured with microwaves propagating parallel to the fast neon beam. The resonance is a composite of two partially resolved spin components, whose relative positions and strengths are represented by the vertical bars, as obtained from the calculation described in the text. The smooth curve is a fit, from which the spinless transition frequency is determined.

optical lines in Fig. 2. Locating the transition can be more difficult. For example, from Fig. 2, it could be estimated that the $10H_{11/2}-10I_{13/2}$ interval is approximately 0.045 cm^{-1} , or 1350 MHz, but since the linewidth of the microwave resonances is much smaller than this, some searching is required to locate the resonance. The microwave resonances can be observed using only the single laser at 4 in Fig. 1, but in most cases the signal size could be increased by exaggerating the natural population difference between the two levels of the microwave transition with an initial laser interaction at 2 in Fig. 1. This laser would be Doppler tuned to excite to $n=27$ the less populated of the two levels, thus increasing the population difference between the $n=10$ levels and the size of the microwave-induced population change. This is the same technique used in previous studies of helium [6]. Sixteen different microwave transitions were studied this way and are listed in Table I. The transitions are numbered for each reference [11]. Figure 3 shows the $n=10$ Rydberg fine structure for $5 \leq L \leq 8$, and illustrates the 16 transitions studied. Two types of microwave interaction regions were used for these studies, both of which are described fully in Ref. [7]. Transitions with frequencies below 2 GHz were observed using a TEM transmission line, while for those with frequencies between 3.5 and 5 GHz a G -band waveguide region was used. In both cases, the direction of microwave propagation was parallel to the atomic beam velocity, and resonances were measured for both directions of microwave propagation to eliminate the effects of Doppler shifts.

Figure 4 illustrates a typical microwave resonance signal, transition 12 from Table I. The resonance linewidth is about 1.6 MHz for this TEM interaction region, as determined by the transit time through the region. (The waveguide region gave a slightly larger linewidth of 2.5 MHz.) For the resonance of Fig. 4, this gives a partial resolution of a finer level of structure associated with the Rydberg electron's spin. The two levels with total angular momenta of

$$\vec{J} = \vec{K} \pm \vec{S}_R$$

differ in energy by a few MHz, and as a result there are two allowed transitions ($\Delta J = \Delta K$) which occur at slightly different frequencies. The interactions which cause this splitting

are mostly magnetic, and are discussed in detail below. Since they are weak, their contribution to the energy can be written as

$$\Delta E_{\text{spin}}(L, K, J) = a(L, K) \vec{K} \cdot \vec{S} \quad (1)$$

and consequently the center of gravity of the levels with the two possible values of J is unchanged by the spin interactions. We refer to this center of gravity as the "spinless" level position, and aim at extracting the intervals separating these spinless positions from fitting the microwave resonance data.

These fits were carried out using calculated values of the constants $a(L, K)$ to predict the position of each of the two allowed transitions relative to the spinless interval. Since the microwave transitions were saturated, it was more difficult to predict the relative strength of these two transitions. For simplicity, we assumed that the signal heights were proportional to the statistical weight of the lower- K level of the transition. With this assumption and the calculated positions, even the unresolved composite lines could be fit to extract the spinless interval. As a check on this procedure, the four transitions with the best resolution of the spin structure, 7, 8, 12, and 16, were also fit with an alternative method in which both the relative heights of and the splitting between the two spin components was allowed to vary in the fit. From a study of the results of these fits, which are tabulated in the Appendix, it was concluded that the line splittings agreed to within a few percent with calculations, but that the relative signal heights could vary by 10–20% from the assumed statistical values. At least part of this height variation appeared to be due to drift in the signal size during the period of the frequency scan (about 30 min). We estimated that such drifts could cause an error in the spinless interval of about 5% of the component splitting, and have assigned an additional error to account for this and any other errors in the procedure of extracting the spinless interval from the unresolved spectra.

Microwave resonances were measured for both directions of microwave propagation, and the fitted spinless intervals were combined in a geometric mean to estimate the frequency interval for a stationary atom. These results are shown in column 3 of Table I, with the statistical error from the fits shown in column 4. Column 5 shows the additional error assigned due to the unresolved spin structure, as discussed above. Column 6 shows a final source of experimental uncertainty, due to possible Stark shifts arising from stray electric fields. Previous microwave spectroscopy in Rydberg states of the helium atom, using similar microwave regions have demonstrated that stray fields as large as 0.2 V/cm can be present within the interaction regions [6]. Lacking any procedure for measuring these stray fields in this experiment, we choose to assign an additional uncertainty corresponding to the Stark shift that such a field would produce. The final column of Table I shows the quadrature sum of the three sources of uncertainty for each measured interval. Since no one signal source of error dominates for most of the intervals, we choose to treat these total errors as uncorrelated random errors in the computations that follow.

Figure 3 illustrates that the 16 measured fine-structure intervals directly determine the relative positions of the 15 fine-structure levels pictured there. Since the absolute ener-

TABLE II. Energies of $n=10$ Rydberg states of neon. Column 2 gives the energy of the 14 $n=10$ fine-structure levels identified in column 1, as determined by addition of the measured fine structure intervals of Table I, with the (arbitrary) choice of the $(\frac{3}{2})10K_{15/2}$ state's energy as zero. Columns 3 and 4 give the second-order energy and relativistic correction for each state, as discussed in the text. Column 5 is column 2 less the sum of columns 3 and 4.

State	E_{obs} (MHz)	E^2 (MHz)	E^{Rel} (MHz)	$E - E^2 - E^{\text{Rel}}$
$(\frac{3}{2})10H_{9/2}$	-145.58(77)	-9.18(34)	-18.71	-116.69(84)
$(\frac{3}{2})10H_{11/2}$	2142.67(10)	-15.49(50)	-18.71	2176.87(51)
$(\frac{3}{2})10H_{13/2}$	-6022.24(19)	-15.95(49)	-18.71	-5987.58(52)
$(\frac{3}{2})10I_{9/2}$	-5267.15(35)	7.50(23)	-13.81	-5260.84(42)
$(\frac{3}{2})10I_{11/2}$	-356.30(24)	-3.02(9)	-13.81	-339.47(26)
$(\frac{3}{2})10I_{13/2}$	800.52(5)	-5.52(16)	-13.81	819.85(17)
$(\frac{3}{2})10I_{15/2}$	-4131.36(15)	-4.98(13)	-13.81	-4112.57(20)
$(\frac{3}{2})10K_{11/2}$	-3838.06(35)	3.96(12)	-10.22	-3831.80(37)
$(\frac{3}{2})10K_{13/2}$	-646.41(8)	-0.75(2)	-10.22	-635.44(8)
$(\frac{3}{2})10K_{15/12}$	0	-1.95(6)	-10.22	12.17(6)
$(\frac{3}{2})10K_{17/2}$	-3205.01(16)	-1.71(5)	-10.22	-3193.08(17)
$(\frac{3}{2})10L_{13/2}$	-3073.14(35)	2.17(7)	-7.47	-3067.84(36)
$(\frac{3}{2})10L_{15/2}$	-883.09(8)	0.05(1)	-7.47	-875.67(8)
$(\frac{3}{2})10L_{17/2}$	-494.04(5)	-0.59(2)	-7.47	-485.98(5)
$(\frac{3}{2})10L_{19/2}$	-2693.41(18)	-0.65(2)	-7.47	-2685.29(18)

gies cannot be determined by measurements of intervals, we choose to define the zero of energy, for the purposes of this report, to coincide with the position of the $(\frac{3}{2})10K_{15/2}$ level. With this choice, the energies of all 14 other levels pictured in Fig. 3 are determined by adding or subtracting the appropriate interval measurements. In the two cases where redundant measurements exist (intervals 13 and 14), a simple average was used to determine the best level energies. The resulting energies of the 15 high- L fine-structure levels of neon are shown in column 2 of Table II. They represent a unique data set, defining the energies of four adjacent high- L manifolds with unprecedented precision, and they express the final experimental result of this study.

We expect that the fine structure of these high- L Rydberg levels will be described by an effective potential which represents the Coulomb interactions between the Rydberg electron and the ion core. A recent discussion of the Rydberg energy levels of neon with $L=3$ and 4 has shown that this approach is quite successful in accounting for the observed energies [8]. For the higher values of L studied here, it should be even more successful, because of the smaller size and more rapid convergence of the terms of the effective potential. Thus we expect the nonrelativistic energy of the high- L Rydberg levels to be given by

$$E = E_r^0 + \langle \psi_r^0 | V_{\text{eff}} | \psi_r^0 \rangle + \sum_{r'} \frac{|\langle \psi_r^0 | V_{\text{eff}} | \psi_{r'}^0 \rangle|^2}{E_r^0 - E_{r'}^0}, \quad (2)$$

where

$$V_{\text{eff}} = - \left[\frac{e^2 \alpha_S}{2r^4} + \frac{\eta}{r^6} \right] - \left[\frac{eQ}{r^3} + \frac{e^2 \alpha_T}{2r^4} + \frac{C_6}{r^6} \right] \frac{X_c^2 \cdot C^2(\Omega_r)}{\begin{pmatrix} J_c & 2 & J_c \\ -J_c & 0 & J_c \end{pmatrix}}, \quad (3)$$

in which r is the Rydberg electron's radial coordinate, and Ω_r is its angular position. X_c^2 is a unit second-rank tensor in the space of the core; i.e., it is a second rank tensor with reduced matrix element equal to 1. $C^2(\Omega_r)$ is a second-rank spherical tensor in the Rydberg electron's angular coordinates [13], and the symbol in the denominator is a $3J$ symbol in which $J_c = \frac{3}{2}$. The coefficients which occur in Eq. (3) are properties of the Ne^+ core. Q is the core quadrupole moment. α_S is the core scalar dipole polarizability. α_T is the core tensor dipole polarizability. η is the parameter representing combined higher-order effects. C_6 is the parameter representing combined higher-order effects. These parameters can, in principle, be calculated directly, but in practice they are more precisely determined by comparison of Rydberg fine structures to the predictions derived from V_{eff} . Equation (2) is of the form of a perturbation expansion, with the first term representing the zeroth-order Rydberg energy; the second term the expectation value of V_{eff} ; and the last term the second-order perturbation due to V_{eff} , which we call E^2 . This last term is of minor importance to the structure of the high- L Rydberg levels studied here, so one way to estimate the parameters listed above would be to first assume that $E^2=0$, and then fit the observed fine structure to determine the parameter values. Subsequently, the fitted parameter values could be used to calculate E^2 , which could be subtracted from the observed structure and the remainder fit to obtain an improved estimate of the core parameters. Because the effects of E^2 are small, this procedure quickly leads to self-consistent choices of the parameters. The second-order terms correspond to energy shifts due to mixing with other Rydberg states, both in the discrete and continuous spectra. They are calculated here using the numerical procedures described elsewhere [14]. Briefly, the contributions to E^2 from bound Rydberg levels with $n \leq 40$ were tabulated explicitly, and the remainder of the discrete contribution was estimated by extrapolation. The continuum con-

TABLE III. Fitted neon structure factors.

State	A_0 (MHz)	A_1 (MHz)	A_2 (MHz)
10H	-2841.11(66)	-1.26(11)	8156.3(1.1)
10I	-2134.72(12)	-0.816(19)	4926.22(24)
10K	-1869.37(8)	-0.557(11)	3200.47(15)
10L	-1756.15(9)	-0.386(8)	2195.55(16)
Interval	ΔA_0 (MHz)		
10I-10H:	706.39(67)		
10K-10I:	265.35(14)		
10L-10K	113.22(12)		

tributions were estimated by calculating a few specific continuum energies in the range 0–0.5 a.u., and estimating the integral over all energies. All these calculations assumed purely hydrogenic radial wave functions. Table II shows the total second-order energy shift calculated for each of the 15 states under study. The error bars shown for these calculations are due partly to the finite number of terms included in the polarization potential, and the resulting finite degree of convergence of the sum [14], partly due to uncertainty in the coefficients in V_{eff} , and partly due to the estimated computational errors. In most cases, the computational error, which we estimate at 3%, dominates [15]. Also shown in Table II are the small relativistic corrections associated with the p^4 term in the Rydberg electron's kinetic energy [6]. Both the second-order energies and the relativistic corrections are subtracted from the experimentally determined fine-structure energies, in order to form a level structure which could be considered to be simply the expectation value of V_{eff} ; i.e., the first term in Eq. (2). For these corrected energies, we expect

$$E_{\text{corr}}(L, K) \equiv E_{\text{obs}} - E^2 - E^{\text{rel}} = A_0 + A_1 \{ \vec{J}_c \cdot \vec{L} \} + A_2 \{ T_{J_c}^2 \cdot T_L^2 \}, \quad (4)$$

with

$$\vec{J}_c \cdot \vec{L} = \frac{[K(K+1) - J_c(J_c+1) - L(L+1)]}{2},$$

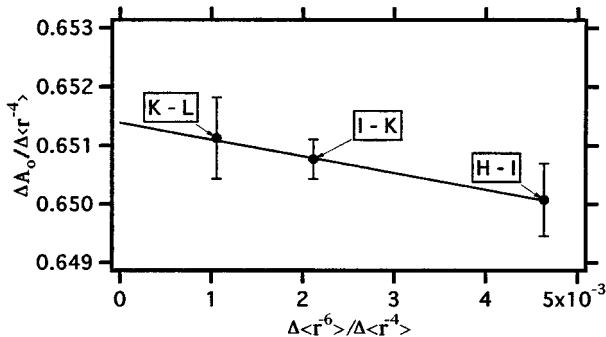


FIG. 5. Ratio of scalar fine-structure intervals to differences in the expectation values of r^{-4} , plotted vs the ratio of $\langle r^{-6} \rangle / \langle r^{-4} \rangle$ for the 10H-I, 10I-K, and 10K-L intervals in neon. The y intercept determines the scalar dipole polarizability of Ne^+ .

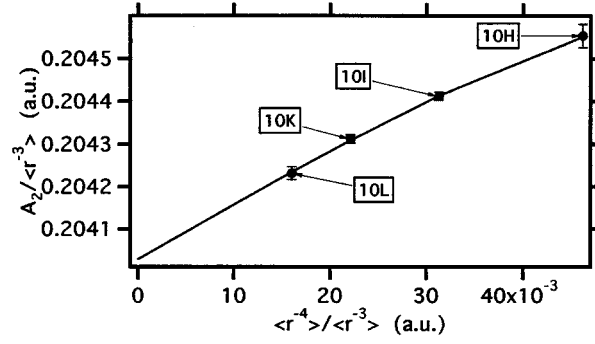


FIG. 6. Tensor fine-structure factors for 10H, 10I, 10K, and 10L states of neon, divided by the expectation values of r^{-3} for those levels. The x axis shows $\langle r^{-4} \rangle / \langle r^{-3} \rangle$ for the same levels. The y intercept of this plot gives the quadrupole moment of Ne^+ , the slope determines the tensor dipole polarizability, and the (very slight) curvature indicates the value of the coefficient C_6 .

$$T_{J_c}^2 \cdot T_L^2 \equiv (-1)^{J_c+K} \begin{Bmatrix} K & L & J_c \\ 2 & J_c & L \end{Bmatrix} \frac{(2L+1) \begin{pmatrix} L & 2 & L \\ 0 & 0 & 0 \end{pmatrix}}{\begin{pmatrix} J_c & 2 & J_c \\ -J_c & 0 & J_c \end{pmatrix}}.$$

We refer to the coefficients A_0 , A_1 , and A_2 as scalar, vector, and tensor structure factors. Actually, according to the form of V_{eff} defined in Eq. (3), A_1 is expected to be zero, but it was impossible to fit the experimental data satisfactorily without a term of this form, and in retrospect its presence is understood to be due mostly to magnetic interactions neglected in deriving Eq. (3). For the 10I, 10K, and 10L states, there are four levels and three parameters, and satisfactory fits are found. The 10H fits are based only on the three measured level positions, and so fit identically. The structure factors found from the fits are shown in Table III.

According to the effective potential model, the scalar structure factor is expected to be given by

$$A_0(nL) = -\frac{e^2 \alpha_S}{2} \langle r^{-4} \rangle_{nL} - \eta \langle r^{-6} \rangle_{nL} + \dots, \quad (5)$$

where

$$\eta \equiv \alpha_Q - 6\beta_d \quad (6)$$

is a parameter combining the effects of adiabatic quadrupole polarizability (α_Q) and nonadiabatic dipole polarizability (β_d) [8]. As a test for possible higher-order contributions, Fig. 5 plots

$$\frac{\Delta A_0}{\Delta \langle r^{-4} \rangle} \text{ vs } \frac{\Delta \langle r^{-6} \rangle}{\Delta \langle r^{-4} \rangle}, \quad (7)$$

where, in this expression, Δ stands for the difference between adjacent L values. The three measured points fall on a good straight line, indicating that higher-order terms do not contribute significantly. Fitting to a straight line yields estimates of the parameters contributing to A_0 :

$$\alpha_S = 1.3028(13)a_0^3, \quad \eta = -0.29(24)e^2 a_0^5.$$

The tensor structure factor is expected to be given by

$$A_2 = -eQ\langle r^{-3} \rangle - \frac{e^2\alpha_T}{2}\langle r^{-4} \rangle - C_6\langle r^{-6} \rangle. \quad (8)$$

Q is the quadrupole moment, and α_T the tensor component of the dipole polarizability [16]. The constant C_6 represents the net effect of tensor contributions from quadrupole-quadrupole and dipole-octupole adiabatic polarizability and nonadiabatic dipole-dipole polarizability, none of which have been calculated for this core ion. To the extent that the contributions from C_6 are negligible, the ratio of A_2 to $\langle r^{-3} \rangle$ should fit a straight line when plotted versus $\langle r^{-4} \rangle / \langle r^{-3} \rangle$. Such a plot, shown in Fig. 6, does indeed indicate that the contributions of C_6 are very small. A fit of the measured values of A_2 for the H , I , K , and L states determines the following values of the tensor core parameters:

$$Q = -0.204\,03(5)ea_0^2, \quad \alpha_T = -0.026(5)a_0^3, \\ C_6 = 0.5(5)e^2a_0^5.$$

The existence of significant vector structure (A_1) is *not* predicted by the effective potential model, but is nevertheless clearly present, as shown by the fitted A_1 's in Table III. Since, however, the fitted vector coefficients are much smaller than the scalar or tensor structure factors, we are led to reexamine magnetic effects, neglected up to now. The careful study of magnetic interactions in high- L states of helium [17] provides an instructive analogy. In that case, it was found to be a good approximation to ignore the details of the core wave function and to represent the magnetic effects of the core by a point magnetic dipole with magnitude

$$\vec{\mu}_c = \mu_0 g_J \vec{J}_c. \quad (9)$$

If the same approximation is valid for neon high- L Rydberg levels, we expect that an adequate representation of magnetic interactions should be

$$H_{\text{MFS}} = \alpha^2 \left[\frac{1}{2} \frac{\vec{L} \cdot \vec{S}_R}{r^3} - \frac{g_J}{2} \frac{\vec{L} \cdot \vec{J}_c}{r^3} + \frac{g_J}{2} + \frac{\vec{J}_c \cdot (1 - 3\hat{r}\hat{r}) \cdot \vec{S}_R}{r^3} \right] \text{ a.u.} \quad (10)$$

The terms involving S_R , the Rydberg spin, will contribute to the small splitting between the two states of common L and K , such as

$$\left(\frac{3}{2}\right)10H_{13/2}(J=6,7) \quad \text{where } \vec{J} = \vec{K} + \vec{S}_R.$$

There is some experimental evidence of splittings of this type in the partially resolved spin components displayed in several of the microwave transition spectra, such as that illustrated in Fig. 4. It is also expected, however, that these spin splittings will reflect any exchange energies due to the required antisymmetrization of the total electronic wave function. With only one unpaired core spin, the exchange energies can be parameterized just as in the helium atom [17]:

$$H_X = -V_X \left[2(\vec{S}_R \cdot \vec{S}_c + \frac{1}{4}) \right] = \mp V_X (S_T = 1, 0). \quad (11)$$

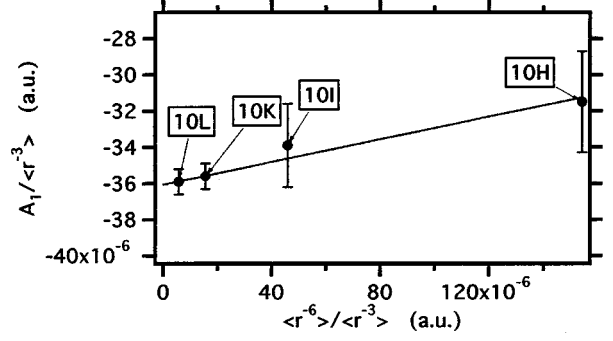


FIG. 7. Vector structure factors for the 10H, 10I, 10K, and 10L states of neon, divided by the expectation value of r^{-3} for each level, and plotted vs $\langle r^{-6} \rangle / \langle r^{-3} \rangle$. The y intercept gives the g value of the Ne^+ ground state, to the extent that the simplified model of Rydberg magnetic structure is valid. Any contribution of the form predicted to result from geometric phase effects would be reflected in the slope of the plotted points.

The combined effects of H_{MGS} and H_X , both treated as small perturbations, are

$$\langle H_{\text{MFS}} + H_X \rangle = -\frac{g_J}{2} \alpha^2 \frac{\vec{J}_c \cdot \vec{L}}{r^3} - \frac{V_X}{2} + [a_{\text{MFS}}(L, K) + a_X(L, K)] \vec{K} \cdot \vec{S}_R. \quad (12)$$

The last term in this expression gives rise to the spin splittings in the microwave spectra. By the comparison with the measured splittings discussed in the Appendix, it can be determined that an adequate account of the experimental observations is obtained by setting V_X (and therefore also a_X) equal to zero, i.e., by completely neglecting exchange ef-

TABLE IV. Ne^+ core parameters from experiment and theory. Column 2 shows the results of this study. Column 3 shows the values found in a previous study of Rydberg F and G states. Column 4 shows theoretical values, when they exist. * represents values *assumed* in the analysis of Ref. [8].

Property	Present work	Previous expt.	theory
$Q(ea_0^2)$	-0.204 03(5)	-0.2030	-0.1964 ^a -0.2032(5) ^b -0.2117 ^c
$\alpha_S(a_0^3)$	1.3028(13)	1.310	1.27 ^d
$\alpha_T(a_0^3)$	-0.026(5)	-0.035*	-0.035 ^e
g_J	1.354(21)		
$\eta(e^2a_0^5)$	-0.29(24)	-1.44*	-1.44 ^f
$C_6(e^2a_0^5)$	0.5(5)	0*	
$C_\phi(e^2a_0^5)$	0.031(19)		1 a.u. (?) ^g

^aHartree-Fock, cited in Ref. [19].

^bMulticonfiguration Hartree-Fock [19].

^cRelativistic many-body perturbation theory [21].

^dHibbert [22].

^eHibbert [23].

^fCited in Ref. [8].

^gOrder-of-magnitude estimate [18].

fects. Even for the lowest L state studied, the $10H$ state, this comparison rules out values of V_X as large as 0.1 MHz for any of the levels studied.

The first term in Eq. (12) represents a predicted vector contribution to the high- L fine structure, arising from the interaction between the core magnetic moment and the magnetic field created at the core by the motion of the Rydberg electron. For the $^2P_{3/2}$ core state, in pure LS coupling, we expect $g_J = \frac{4}{3}$. This predicts vector structure quite comparable to the observations summarized in Table III. A vector structure of a rather different type was recently predicted to arise from consideration of “geometric phase” effects on the motion of a nonpenetrating Rydberg electron moving in the field of a core with nonzero angular momentum [18]. This effect, which has never been observed experimentally, was predicted to give a vector structure proportional to the inverse sixth power of the Rydberg radial coordinate and with a coefficient which is on the order of an atomic polarizability. To allow for the possibility that the measured vector structure factors contain contributions of both types, we take

$$A_1(L) = -\frac{g_J}{2} \alpha^2 \langle r^{-3} \rangle + C_\phi \langle r^{-6} \rangle \quad (13)$$

and fit the observed vector structure factors to determine both g_J and C_ϕ . The results of this fit, illustrated in Fig. 7, are

$$g_J = 1.354(21), \quad C_\phi = 0.031(19) \text{ a.u.}$$

The fitted value of g_J is consistent with the pure LS coupling value of $\frac{4}{3}$. The fitted value of C_ϕ is less than two standard deviations from zero, and considerably smaller than might have been expected based on the published estimate that C_ϕ should be “on the order of an atomic polarizability” [18]. To our knowledge, this is the first measurement of an effect of this type, and no more detailed theoretical calculations are yet available. When such calculations are done, it will be interesting to see whether Ne^+ is a special case where this effect is unusually small. Experimental studies which explore this effect in other high- L Rydberg systems should also be possible using the techniques of the present measurement.

Table IV compares the values of the leading core parameters Q , α_S , and α_T obtained from the present measurements with those reported previously based on the study of $L=3$ and 4 Rydberg levels of neon [8], and with theoretical values. The value of α_S found here is about 0.5% smaller than the value found in the study of neon f and g levels [8]. The higher value found there is partially due to the assumption of a calculated value of the parameter η is that analysis, $\eta = -1.44$, which is considerably larger than the value indicated by the present measurements. Since the present analysis avoids reliance on any calculated values, and instead extracts α_S and η simultaneously from the pattern of high- L data, it should be much more reliable. The fitted values of α_S and α_T are both consistent with calculated values to within about 2% of α_S . This probably indicates the level of accuracy of the existing calculations. Note that the present measurements are at least an order of magnitude more precise so they could be used to test improved calculations.

The value of the Ne^+ quadrupole moment Q found from the present measurements is 0.5% larger than the value re-

TABLE V. Values of the spin structure coefficients a_{MFS} and a_x for the levels involved in the four transitions with the best-resolved spin structure. For each transition, the first listed level has the higher energy.

Transition	Level	a_{MFS} (MHz)	a_x
7	$I_{15/2}$	0.650	$-0.133V_X(10I)$
7	$H_{13/2}$	1.068	$-0.154V_X(10H)$
8	$K_{17/2}$	0.424	$-0.118V_X(10K)$
8	$I_{15/2}$	0.650	$-0.133V_X(10I)$
12	$I_{13/2}$	0.567	$-0.072V_X(10I)$
12	$K_{13/2}$	0.356	$0.024V_X(10K)$
16	$K_{15/2}$	0.382	$-0.060V_X(10K)$
16	$I_{15/2}$	0.650	$-0.133V_X(10I)$

ported in Ref. [8] from study of F and G states of neon. However, this relatively small difference again appears in part to be fortuitous since in the analysis of Ref. [8] the parameter α_T was assumed to be equal to its calculated value -0.035 , an assumption which significantly affects the fitted value of Q . Again, in this study we avoid any reliance on calculated values by fitting the pattern of data in a range of L states, and simultaneously extract Q , α_T , and even the higher-order coefficient C_6 . Thus the present study should give a much more reliable result. Theoretical calculations of Q are within 4% of the measured value, with the most accurate calculation to date being the multiconfiguration Hartree-Fock calculation of Sundholm and Olsen [19].

The predictive power of the effective potential model is illustrated by the fact that, now that the four parameters Q ,

TABLE VI. Results of the alternate fits of the four transitions with the best-resolved spin structure. The parameter $\delta\nu$ measures the splitting between the two spin components, and the parameter r is the relative strength of the component with less statistical weight. In the constrained fits, such as carried out for all the transitions, these were fixed at the values marked with * in the table. In the alternate fits, these parameters were both free to vary, and resulted in the fitted values shown. The two fits for each transition are from data with microwave propagation direction parallel (p) or antiparallel (a) to the beam velocity. The average values of the fitted parameters for these two fits are also shown for each transition.

Transition	$\delta\nu$ (MHz)	r
7	2.273*	0.867*
7p	2.207(74)	0.633(67)
7a	2.188(94)	0.956(120)
7AV	2.198(60)	0.795(60)
8	1.383*	0.882*
8p	1.500(24)	1.073(46)
8a	1.453(23)	1.250(50)
8AV	1.477(17)	1.162(68)
12	1.477*	0.867*
12p	1.533(44)	0.691(56)
12a	1.453(58)	0.737(78)
12AV	1.493(36)	0.714(96)
16	2.149*	0.882*
16p	2.140(69)	0.662(64)
16a	2.100(66)	0.641(54)
16AV	2.120(48)	0.652(42)

α_S , α_T , and g_J are known, and the size of higher-order contributions is limited by the estimates of the parameters η , C_6 , and C_ϕ , other high- L Rydberg level structures in the neon atom can also be predicted using the same core parameters. This can lead to reliable predictions of emission spectral lines in many different regions of the spectrum. At the same time, the core parameters themselves represent valuable information which can be used to test improving atomic structure calculations. Even these four parameters represent a far larger and far more precise data set than is usually available for the ground state of neutral atoms, where the only available information is usually the binding energy (to some degree of precision), a g factor, and perhaps one or two hyperfine coupling constants. The binding energy is insensitive, in first order, to configuration-interaction effects, and the hyperfine constants measure only certain limited characteristics of the wave function, such as its value at the origin. The quadrupole moment and dipole polarizabilities represent significant additional information. The quadrupole moment is especially sensitive to long-range and configuration-interaction effects [20], but is a property which has been difficult to measure precisely for neutral atoms.

ACKNOWLEDGMENTS

This work was supported by the National Science Foundation under Grant Nos. PHY90-19064 and PHY93-96235.

APPENDIX

As a check on the procedure used to extract the spinless fine-structure intervals from fits of the partially resolved composite line shapes consisting of two spin components,

the four resonances with the best resolution of the spin components were also fit with an alternative method. Table V lists the four transitions so studied, and tabulates the values of the spin structure coefficients, a_{MFS} and a_X discussed in the text. The spin component splittings, neglecting exchange, may be calculated from a_{MFS} . Table VI shows the results of the alternative fits of these resonance line shapes. In the normal fits, the values of the two parameters $\delta\nu$ and r which represent, respectively, the spin component splitting and the relative strength of the lower statistical weight line, were fixed at the values marked by * in Table VI. In the alternative fits, both these parameters were allowed to vary freely. Table VI shows the fitted values of these two parameters from fits of each transition for both directions of microwave propagation. Also tabulated are the average values from the two directions of propagation for each line.

The fitted splittings are in agreement to within a few percent with the calculated values. From this we conclude that magnetic interactions alone account for the differences in energy between the nearly degenerate $J=K \pm \frac{1}{2}$ levels. The agreement limits the possible size of the exchange energy parameters V_X to be less than 0.1 MHz for $10H$, $10I$, and $10K$ levels, making the exchange energies completely negligible for this experiment.

The fitted relative strengths are in much poorer agreement with the assumed statistical weights, sometimes differing by as much as 20%. Additional fits were carried out to assess the impact of such an error on the fitted spinless interval for transitions where the spin components were unresolved. It was concluded that an additional error of 5% of the component splitting would account for the uncertainty in relative component strengths.

-
- [1] E. S. Chang and H. J. Sakai, *J. Phys. B* **15**, L649 (1982).
 [2] F. J. Murcray *et al.* *Astrophys. J.* **247**, L97 (1981); J. Brault and R. Noyes, *ibid.* **269**, L61 (1983).
 [3] E. S. Chang and R. W. Noyes, *Ap. J.* **275**, L11 (1983).
 [4] M. A. Geller (unpublished).
 [5] W. G. Shoenfeld, Ph.D. thesis, University of Massachusetts, 1994 (unpublished).
 [6] E. A. Hessels, P. W. Arcuni, F. J. Deck, and S. R. Lundeen, *Phys. Rev. A* **46**, 2622 (1992).
 [7] W. G. Sturuss, E. A. Hessels, P. W. Arcuni, and S. R. Lundeen, *Phys. Rev. A* **44**, 3032 (1991).
 [8] E. S. Chang, W. G. Shoenfeld, E. Biemont, P. Quinet, and P. Palmeri, *Phys. Scr.* **49**, 26 (1994).
 [9] The ion source is a hot filament type source, Model AIM-210 manufactured by Accelerators, Inc.
 [10] Unlike the other lines in the spectrum, the X lines do not appear in the same relative position for transitions near the frequency of 10–30 hydrogenic transition. They probably correspond to excitation of $n \neq 10$ levels with a large quantum defect.
 [11] R. F. Ward, Jr., Ph.D. thesis, University of Notre Dame, 1994 (unpublished).
 [12] C. Yamada, H. Kanamori, and E. Hirota, *J. Chem. Phys.* **83**, 552 (1985).
 [13] A. R. Edmonds, *Angular Momentum in Quantum Mechanics* (Princeton University Press, Princeton, NJ, 1957).
 [14] P. W. Arcuni, E. A. Hessels, and S. R. Lundeen, *Phys. Rev. A* **41**, 3648 (1990).
 [15] We wish to point out that in the calculation of E^2 the matrix element of the quadrupole moment operator (X_c^2) between the $^2P_{3/2}$ and $^2P_{1/2}$ core states was *approximated* by assuming pure LS coupling. In this approximation, both diagonal and off-diagonal reduced matrix elements of X_c^2 are equal to 1. We believe this is unlikely to lead to errors larger than the 3% numerical precision of the E^2 calculations.
 [16] J. R. P. Angel and P. G. H. Sandars, *Proc. R. Soc. London Ser. A* **305**, 125 (1968); J. R. P. Angel, P. G. H. Sandars, and G. K. J. Woodgate, *J. Chem. Phys.* **47**, 1552 (1967).
 [17] E. A. Hessels, W. G. Sturuss, S. R. Lundeen, and David R. Cok, *Phys. Rev. A* **35**, 4489 (1987).
 [18] B. Zygelman, *Phys. Rev. Lett.* **64**, 256 (1990), Eq. 23.
 [19] D. Sundholm and J. Olsen, *Phys. Rev. A* **49**, 3453 (1994).
 [20] P. G. H. Sandars and A. J. Stewart, in *Atomic Physics 3*, edited by S. J. Smith and G. K. Walters (Plenum, New York, 1973), p. 429.
 [21] Z. W. Liu (private communication), using relativistic many-body perturbation theory.
 [22] A. Hibbert, M. Le Dourneuf, and Vo Ky Lan, *J. Phys. B* **10**, 1015 (1977).
 [23] A. Hibbert (private communication), cited in Ref. [8].